steel research international

steel research international

RESEARCH ARTICLE OPEN ACCESS

Phase Transformation Behavior of Continuously Cooled Fe–C–V–(Mo) Alloys

Anastasiya Tselikova[1,2] | Jannik Zuraszek[1] | Ulrich Krupp[1] | Rolf Schmidt[2] | Hardy Mohrbacher[3,4] | Alexander Gramlich[1]

[1]Steel Institute of RWTH Aachen University, Aachen, Germany | [2]Vantage Alloys AG, Zug, Switzerland | [3]NiobelCon, Schilde, Belgium | [4]Department of Materials Engineering (MTM), KU Leuven, Leuven, Belgium

Correspondence: Anastasiya Tselikova (anastasiya.tselikova@vantage-alloys.com)

Received: 24 September 2025 | **Revised:** 20 January 2026 | **Accepted:** 20 January 2026

Keywords: interphase precipitation | molybdenum | phase transformation | vanadium

ABSTRACT

In this study, the effect of vanadium microalloying in simplified ternary Fe–(0.074–0.244 wt%) C–(0.25–1.01 wt%)V and quaternary (+0.2 wt% Mo) alloys on transformation temperatures and hardness is presented. For this matter, dilatometric investigations of the continuous cooling transformation behavior were performed and correlated with the obtained microstructure. It is shown that Widmanstätten ferrite was formed at higher cooling rates, followed by an increase in the polygonal ferrite fraction with decreasing cooling rates. Widmanstätten ferrite has been fully replaced by polygonal ferrite at faster cooling rates as C and V contents increase. Mo addition retards the kinetics of austenite-to-ferrite transformation and leads to a reduced hardening effect during continuous cooling. The more significant hardening at a ferrite finish temperature of 650°C with rising C and V contents, combined with the nearly suppressive effect on pearlite formation and in-row precipitates observed in scanning electron microscope, supports the presence of a large volume fraction of vanadium interphase precipitates.

1 | Introduction

Within several industrial applications, high-strength steels are under constant investigation and development. The reduction of environmental impact and energy consumption during application is mainly achieved by the application of lightweight steel designs to achieve the decarbonization trend requirements [1–4]. The strength of steel can be increased significantly to levels exceeding that of advanced light alloys [5–11] by using different alloying and processing concepts. Nevertheless, this leads to an opposite effect, since the intensive extraction of alloying elements and complex thermomechanical processes leads to an increase of environmental impact [12]. Therefore, the focus of lightweight design of steel components usually lies on downgauging, improvement of strength, density, and/or elongation, leading to weight reduction [13]. However, stiffness, as another important design factor, is most often not considered [13]. This property is expressed by Young's modulus (E) and it is assumed as a given intrinsic property that cannot be marginally modified either by alloying additions or by mechanical or thermal processing [8]. Steels with high strength can still lack sufficient formability, i.e. stiffness against small deformation such as bending, buckling, and deflection in thin-walled components [13–16]. Therefore, the realization of lean-alloyed steels with higher modulus and excellent strength and ductility indicators are of great economic interest [13, 17, 18]. Therefore, nanoscaled interphase precipitation (IP) has attracted great interest as a strengthening mechanism to achieve the optimal combination of above-mentioned mechanical properties through the strain fields caused by coherent precipitates in a ferritic matrix [19–23]. The uniqueness of vanadium carbonitrides V(C, N) lies on its atomic volume (misfit volumes) in ferritic bcc crystals, giving it a minimum misfit within ferrite. This lower misfit leads to low coarsening susceptibility when compared to other inclusions [24, 25]. This is fundamental, especially for high-temperature application, since the elastic modulus decreases with increasing

temperature [19, 25]. The addition of molybdenum has been shown to reduce austenite-to-ferrite transformation kinetics, the ferritic grain size, and the precipitate size in vanadium-containing steels in isothermal holding conditions [26]. In order to achieve steels with higher elastic modulus balanced with high strength and ductility through coherent precipitates, an understanding of the phase transformation is needed by optimizing the alloy design and process. In continuously cooled low-carbon steels, the dominant decomposition product of austenite is ferrite [27, 28]. Very different cooling rates can affect not only kinetics but also the sequence of phase transformations [29]. The precipitation of vanadium carbide (VC) takes place either during the austenite-to-ferrite phase transformation at the migrating austenite/ferrite interface, forming IPs, or in the ferrite phase as random precipitates. Vanadium (V) and carbon (C) solubility are high in austenite but low in the ferrite phase, dropping during austenite-to-ferrite transformation, giving rise to IP [30]. Those IP are formed by repeated nucleation of particles in the austenite/ferrite interface as the transformation front moves through austenite [20] and their diameter is typically only a few nanometers [31]. The number density of alloy carbides can be formed by adding more carbide-forming elements [32, 33]. Therefore, VC can be selectively precipitated by controlled heat treatment of a steel alloyed with C and V [34]. Those coherent precipitates in a ferritic matrix would fulfill the above-mentioned goals; however, studies on the elastic modulus in combination with the above-mentioned mechanical properties, especially in purely V- and Mo-microalloyed steels, are rare [35]. Therefore, the present study aims to investigate the effect of vanadium microalloying on phase transformation behavior of simplified ternary and quaternary alloying systems. This is the first step toward understanding how to promote the best combination of higher strength, ductility, and elastic modulus through IP in a ferritic matrix. Particularly, the influence of vanadium and molybdenum on transformation temperatures and macroscopic hardness were evaluated, since the synergy of both microalloying elements in continuously cooled steels was never studied before, especially in purely V- and Mo-microalloyed alloys. This is the first step of our work to achieve steels with higher strength and ductility while also maintaining and even slightly enhancing the elastic properties through IP in a ferritic matrix.

2 | Materials and Methods

To investigate the phase transformation behavior of vanadium-alloyed steels, four high-purity laboratory melts were produced using different compositions, which are shown in Table 1. The chosen chemical composition had into account the stoichiometry and molar fraction of V and C, so that the effect of C and V contents could be analyzed in light of IP potential. The raw material was first melted in a vacuum induction furnace and then cast into ingots of ≈80 kg with dimensions of 140 × 140 × 1000 mm (H × W × D). The blocks were then soaked at a furnace temperature of 1200°C for a period of 2 h, followed by forging to size 60 × 60 mm.

TABLE 1 | Chemical composition (wt pct) of the investigated steels.

	C	Mo	V	N, ppm
V25	0.074	—	0.25	<10
V50	0.130	—	0.49	<10
V50Mo	0.126	0.2	0.48	<10
V100	0.244	—	1.01	<10

Continuous cooling transformation (CCT) diagrams of the four sample compositions were experimentally determined by the following procedure. Samples were heat treated in a dilatometer, then examined metallographically, and finally tested for hardness (HV). Equilibrium temperatures (A1 and A3) were additionally determined using Thermo-Calc commercial software using the database TCFE11. The dilatometer tests were carried out and evaluated in accordance with the guidelines of the steel-iron test sheet (SEP) 1681 using a quenching dilatometer TA Instruments Dil-805A/D. For the dilatometer tests, up to 15 rectangular samples of each alloy composition were cut and then ground to size of 7.0 × 4.0 × 1.3 mm (L × W × T). The first sample was used to determine the Ac1 and Ac3 temperatures of the alloy composition. For this purpose, the sample was heated to 1200°C in the dilatometer during 30 min by applying near equilibrium heating rates (0.05 Ks^{-1}), while the change in length was detected, followed by a cooling at the same near equilibrium cooling rates (0.05 Ks^{-1}). The determined temperatures were then used as the basis for determining the austenitization temperature above the Ac3 temperature for the subsequent tests. The austenitization temperatures used for V25, V50, V50Mo, and V100, selected according to the measured Ac3, are, respectively, 1030°C, 1000°C, 1010°C, and 990°C. For the determination of the CCT diagrams, different cooling rates were applied as defined by the respective standard DIN EN ISO 643, after heating at 3 Ks^{-1} and holding for 10 min. The three fastest cooling were achieved by applying varying gas flow pressures of helium and argon, while the rest of the samples were cooled with a specified $t_{8/5}$ (cooling time in seconds to cool from 800°C to 500°C, representing the interval for the most critical microstructural changes). The detailed cooling rates and $t_{8/5}$ are shown in appendix Tables A1–A4. To assess microstructure, all dilatometer samples were ground, polished, and etched (Nital). Light microscopy examination was conducted with Leica DM2500 M light microscope. Image analysis software ImageJ was used to measure the exact surface area fraction of a phase on the prepared sample surface. The dilatometer samples were then tested for hardness using Vickers hardness test according to DIN EN ISO 6507 with a force of 98 N for all samples. Thermo-Calc software was used to calculate the precipitation of second phases at equilibrium conditions. Selected samples were examined in a Zeiss Sigma field emission scanning electron microscope (SEM) using the In-lens with acceleration voltages of 5–10 KV to reveal submicrometer-sized precipitates.

3 | Results

3.1 | Transformation Behavior

Table 2 lists the Ae1 and Ae3 temperatures obtained by Thermo-Calc, as well as Ac1 and Ac3 temperatures obtained experimentally for each composition. Ac temperatures are higher than the correspondent Ae temperature due to nonequilibrium conditions during heating.

Figure 1 shows the CCT diagrams of all four compositions with the correspondent hardness values for each cooling rate [36]. In

TABLE 2 | Ae1, Ac1, Ae3, and Ac3 temperatures (°C) determined for all compositions.

	Ae1	Ac1	Ae3	Ac3
V25	762	800	895	950
V50	772	804	886	910
V50Mo	780	822	894	929
V100	785	823	885	913

V25, the main transformation microstructure at all cooling rates was a mixture of Widmanstätten ferrite (WF) and bainite (B), including the fastest cooling rate of 300 K/s. At a similar cooling rate, V50, V50Mo, and V100 presented a microstructure composed by martensite and WF/B. The microstructure entirely composed of primary WF/B is starting to be transformed from the third fastest cooling rate in V50Mo and V100. The CCT diagrams share the evolution of the observed type of ferrite formation with decreasing cooling rate, first WF and then PF is formed with increasing proportion. In addition, a fully polygonal ferrite (PF) microstructure is formed at a faster cooling rate with increasing C and V contents. The general tendency for the ferrite-start and -finish temperatures increases with decreasing cooling rate for all the compositions.

Figure 2 shows ferrite transformation interval (defined as the difference between ferritic start temperature and ferritic end temperature) as a function of ferritic transformation start temperature of all compositions. Up to a transformation start temperature of around 840°C, the ferrite transformation interval stays at around 138 K regardless of C and V contents. At transformation start temperatures higher than 840°C, the ferrite transformation interval decreases at the same rate regardless of V and C contents, reaching its minimum of 40 K for V25 and V100. In V50Mo, there is a high ferrite transformation interval already at

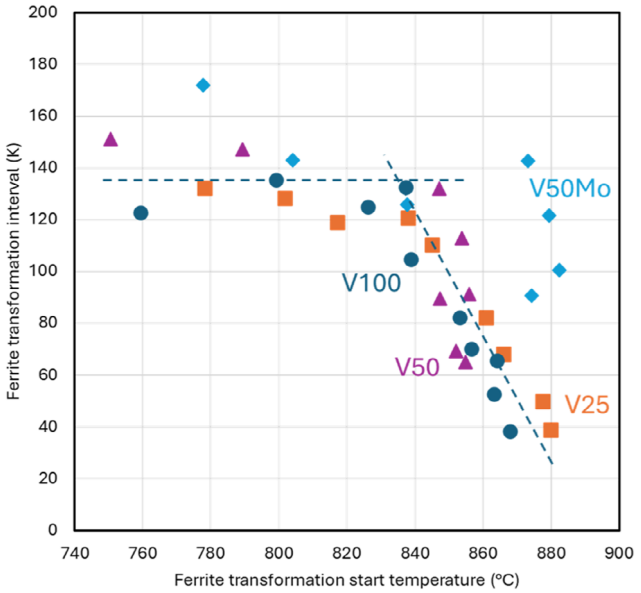

FIGURE 2 | Dependence of ferrite transformation start temperature of each composition with ferrite transformation interval.

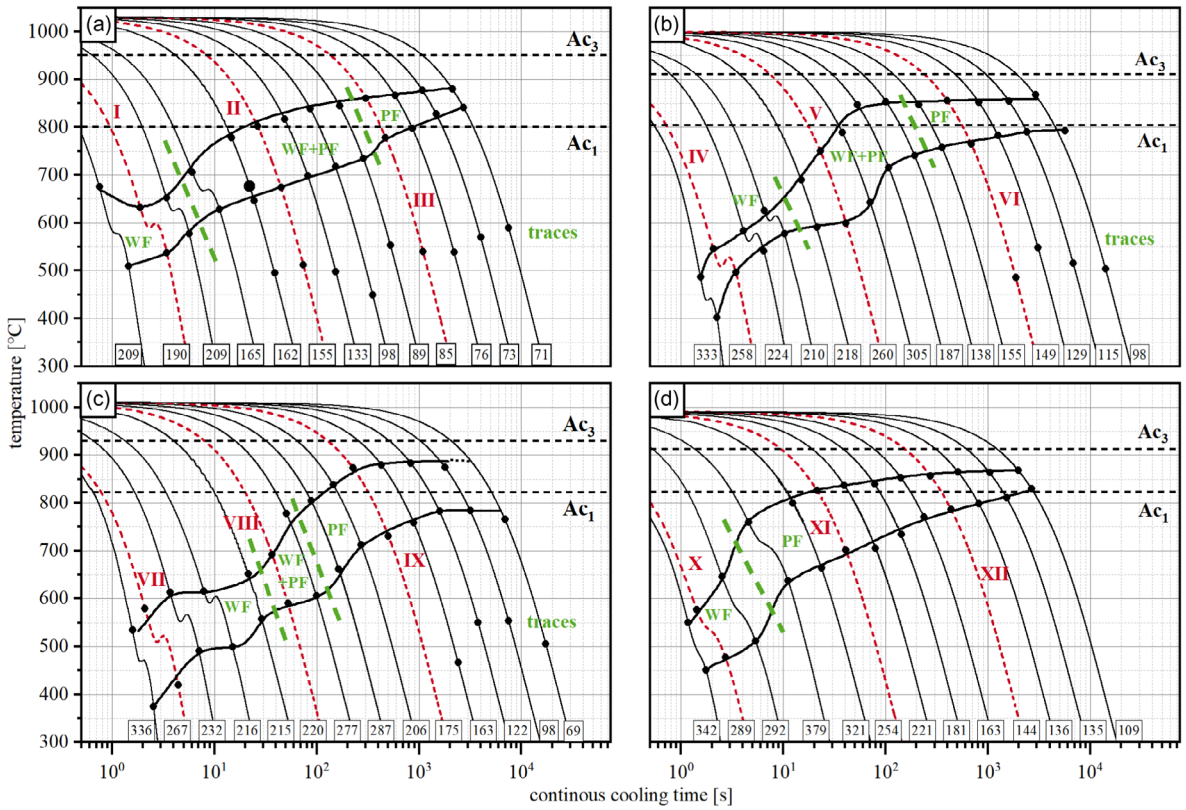

FIGURE 1 | CCT diagrams of V25 (a), V50 (b), V50Mo (c), and V100 (d). The areas with dominantly WF microstructure as well as PF are indicated, as well as the final hardness in Vickers (cf. the rectangles at the end of each cooling rate); microstructures for the dashed cooling curves highlighted in red (numbered I–XII) are shown in Figure (data from [36]). CCT = Continuous cooling transformation; WF = Widmanstätten ferrite; PF = polygonal ferrite.

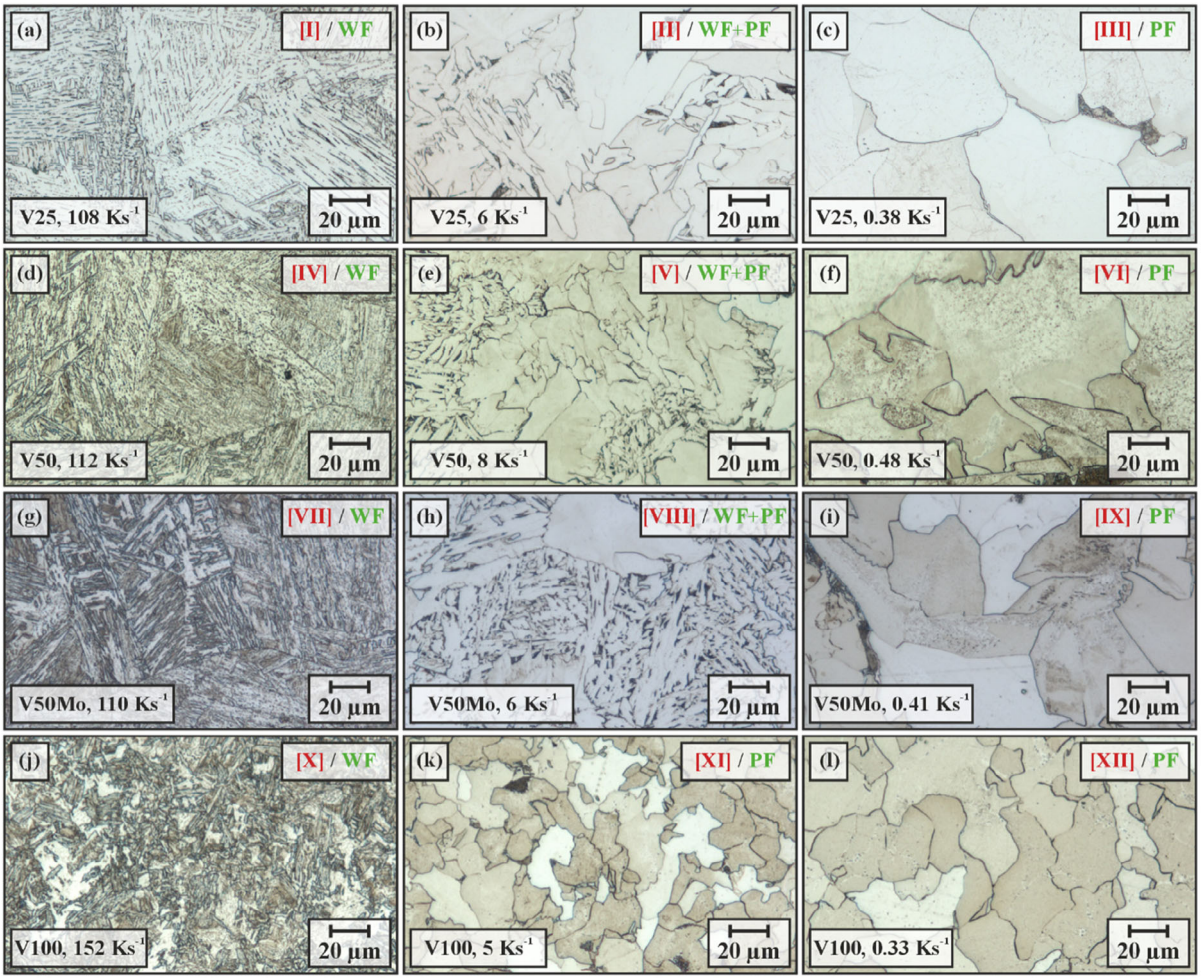

FIGURE 3 | Microstructure based on light optical microscopy of V25 at (a) 108 Ks^{-1}; (b) 6 Ks^{-1}; (c) 0.38 Ks^{-1}; V50 at (d) 112 Ks^{-1}; (e) 8 Ks^{-1}; (f) 0.48 Ks^{-1}; V50Mo at (g) 110 Ks^{-1}; (h) 6 Ks^{-1}; (i) 0.41 Ks^{-1}; V100 at (j) 152 Ks^{-1}; (K) 5 Ks^{-1}; (l) 0.33 Ks^{-1}.

high temperatures (880°C), staying constant for all lower temperatures.

3.2 | Microstructure after Continuous Cooling

3.2.1 | Matrix Phase Constituents

Exemplary micrographs obtained from the samples after continuous cooling are shown in Figure 3. For the highest cooling rates, all compositions presented a mixture of martensite (α'), Widmanstätten ferrite (WF), and bainite (B), except V25, which consists of a mixture of WF and B. For the intermediate cooling rate (5–8 Ks^{-1}), V25 comprises a mixture of WF and B as well as pearlite (P), whereas V50 and V50Mo present a mixture of WF and B and PF without visible appearance of pearlite. On the contrary, V100 presented mainly a PF microstructure with pearlite colonies. At the slowest cooling rate all the compositions contain a fully PF microstructure, in addition to some pearlite colonies visible in V25, V50, and V50Mo (Figure 3).

3.2.2 | Precipitates

Figure 4 represents the variation of precipitates' volume fraction with temperature for all the composition, calculated using

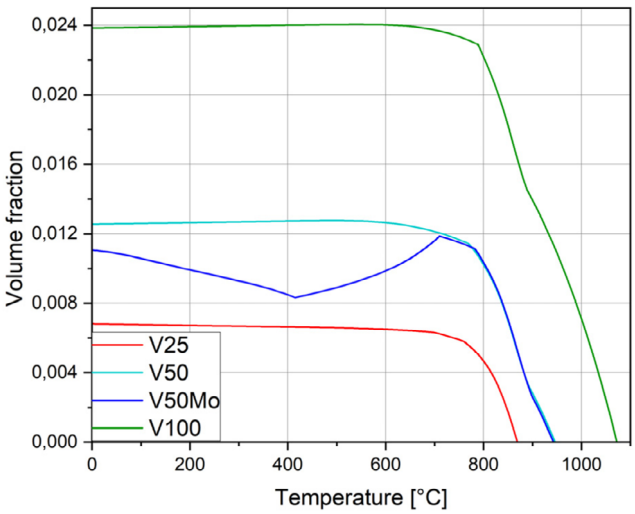

FIGURE 4 | Volume fractions of the precipitates calculated with Thermo-Calc for all compositions.

Themo-Calc. First of all, as the C and V contents increase, the precipitation content increases proportionally. Secondly, the higher the C and V contents, the higher the dissolution

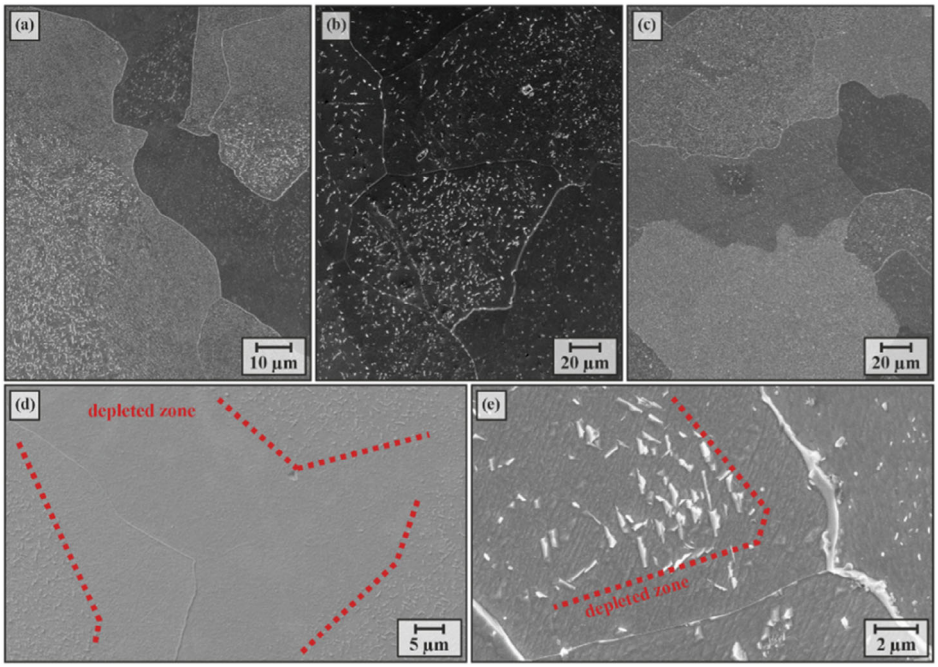

FIGURE 5 | SEM images of samples (a) V50 at 0.03 Ks^{-1}; (b) V50Mo at 0.025 Ks^{-1}; (c) V100 at 0.04 Ks^{-1} and depleted zones of precipitates in sample (d) V50 at 0.03 Ks^{-1}; (e) V50Mo at 0.05 Ks^{-1}. SEM = Scanning electron microscope.

temperature, reaching 869°C for V25, 947°C for V50, and 1073°C for V100. The addition of Mo leads to a lower volume fraction compared to V50 up to 700°C since Thermo-Calc accounts for two types of carbides (represented as *MCTEA* and *FCCA1_#2* in the software) [37].

Scanning electron microscopy was performed to detect the presence of submicrometer-sized precipitates. Exemplary micrographs of steels V50, V50Mo, and V100 treated with the slowest cooling rates are shown in Figure 5. Here, precipitates appear with a bright contrast in a dark matrix due to their higher mass contrast. The morphology of the precipitates revealed different shapes: oval to elongated precipitates; round inclusions observed sporadically with sizes of about 2–3 µm and mainly needle-shaped precipitates were observed in the samples of all compositions, whose lengths range from about 200 to 900 nm. Most of the needles are oriented parallel to each other, with some being perpendicular to each other. Based on energy-dispersive X-ray spectroscopy (EDX) measurement, these needle-shaped precipitates are V-rich in V100 and V- and Mo-rich in V50Mo [36]. Additionally, some accumulation of bigger precipitates surrounded by areas depleted of precipitates are present.

The increase in C or V content appears to lead to a higher density of significantly finer precipitates, which is notable when comparing V50 and V100. On the other hand, the addition of Mo seems to result in fewer but larger precipitates in the microstructure.

3.3 | Cooling Rate Dependence of Vickers Hardness

To reveal a first effect of the precipitates on the mechanical properties, the resulting hardness after continuous cooling can be investigated. In Figure 6, the hardness of all four compositions is plotted as a function of applied cooling rate. The general tendency for hardness of all four compositions is to decrease with the decrease of cooling rate, apart from a peak at medium cooling rate. A particularly pronounced drop in hardness can be observed in V50, V50Mo, and V100 at cooling rates < 300 Ks^{-1}. The hardness of V100 is comparable to those of V50 at the fastest cooling rate, even though the first one has twice as much carbon as the V50. Nevertheless, the hardness peak of V100 is significantly higher in comparison to the other alloys. The opposite behavior was observed in V25, where the hardness is lower overall than that of the other alloys. The addition of molybdenum does not appear to have a significant impact on hardness. However, the peak of V50Mo is shifted to slower cooling rates in comparison

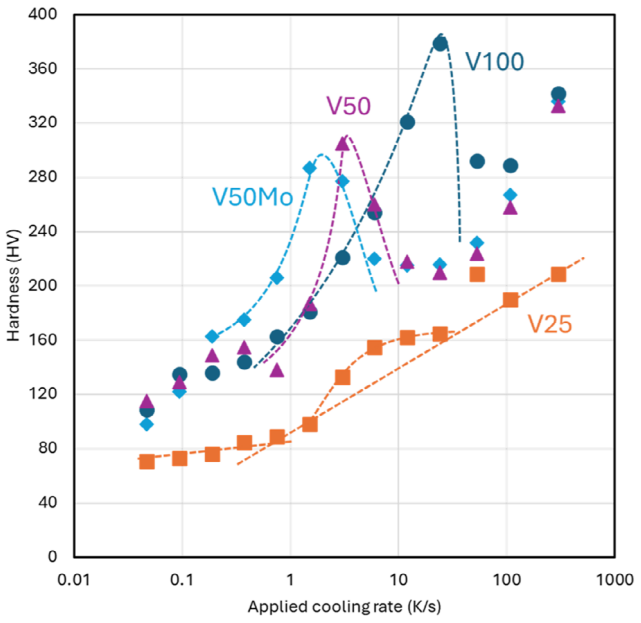

FIGURE 6 | Vickers hardness as a function of applied cooling rate of all compositions.

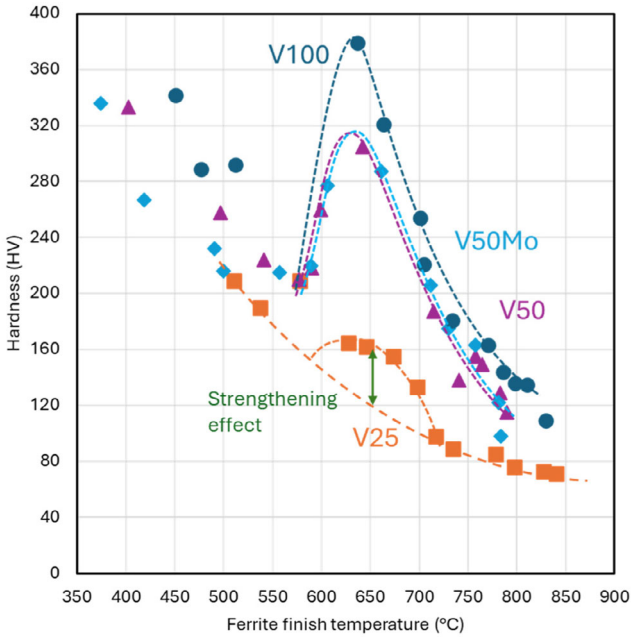

FIGURE 7 | Vickers hardness as a function of ferrite finish temperatures of all compositions.

to the direct reference alloy V50. Additionally, the peak of V50 is slightly higher than that of V50Mo.

Figure 7 shows the hardness of the investigated alloys plotted as a function of ferrite finish temperature according to the CCT diagrams for each composition. It is evident that the hardness peak occurs at the same temperature range around 650°C regardless of carbon, vanadium, and molybdenum contents. However, the maximum hardness is dependent on carbon and vanadium concentration reaching 160 HV for V25 and 380 HV for V100. No difference was observed between the V50 and V50Mo alloys, indicating that the presence of molybdenum is only affecting the precipitation kinetics of VC and does not contribute, in this case, to precipitation strengthening itself.

4 | Discussion

4.1 | Matrix Phase Evolution during Continuous Cooling

The phase transformation in the investigated alloys varies strongly depending on cooling rate and on chemical composition. Even with very fast cooling rates, differences between the materials can be observed. While V25 consists mostly of a mixture of WF and B, all other alloys show a mixture of WF, B, and martensite (Figure 3). Martensite is formed without diffusion by a cooperative shear movement if the diffusion necessary for the transformation into ferrite is hindered due to the very high cooling rate [38]. Additionally, since carbon is an austenite stabilizer, it facilitates the formation of nonequilibrium microstructures such as bainite and martensite and delays ferrite nucleation [39]. However, if the C content is lower, the driving force of the austenite–ferrite transformation increases, promoting the transformation to ferrite at faster cooling rates [38, 40, 41], which explains the lack of martensite in V25. Decreasing the critical cooling rate leads to a gradual transition from the microstructure composed by a mixture of WF and B to PF. This is expected [42], since high cooling rates result in higher undercooling of the austenite, lowering C diffusion, which in turn favors a massive phase transformation that does not require C diffusion over large distances such as WF and B [43, 44]. This behavior inhibits the diffusion-controlled phases like PF, which are formed when the cooling rate is sufficiently low. It nucleates at the austenite grain boundaries and grows toward its center by rejecting carbon into the remaining austenite [39, 45]. For both phases, it is also clear that the microstructure is refined with increasing cooling rate, as already reported [46, 47]. For an equivalent cooling rate, there is a visible refinement of the PF grain size as the C and V contents increase. Additionally, the fully PF microstructure is starting to form for V100 at faster cooling rates (22.00 Ks^{-1}) than for the rest of them, 1.63 Ks^{-1} for V50Mo, 0.45 Ks^{-1} for V50, and 0.37 Ks^{-1} for V25. This behavior is linked to the chosen austenitization temperatures: 161°C, 53°C, and 67°C higher than the calculated precipitates dissolution temperature by Thermo-Calc for V25, V50, and V50Mo, respectively. On the other hand, for V100 the austenitization temperature is 83°C lower than the dissolution temperature. Since Thermo-Calc calculates the dissolution of carbides at equilibrium conditions and the real experimental heating rate is 3 Ks^{-1}, precipitates may still not fully dissolve, because the system needs more time to reach the equilibrium conditions. Therefore, the real dissolution temperature is higher than the calculated one. This shows that from V25 to V100, there is an increased proportion of undissolved carbides after continuous cooling. These undissolved carbides could have reduced the austenite grain size by developing a Zenner pinning effect, which results in a higher number of nucleation sites for polygonal ferrite, leading to the analyzed accelerating effect of its transformation kinetics and its more refined grain size [48]. A general tendency toward an increasing ferritic start and end temperatures with decreasing cooling rate for all the compositions can be also stated. This was expected due to the delay in the onset of austenite–ferrite transformation caused by accelerated cooling [49]. During austenite-to-ferrite transformation during cooling, austenite is known to become more enriched with C. This carbon diffusion governs the speed of the transformation. At higher ferritic start temperature, corresponding to lower cooling rates, carbon diffusivity is high, promoting a higher diffusion rate of C. This is efficient in the kinetics point of view to promote readily interphase VC precipitates during the austenite-to-ferrite transformation, leading to a faster transformation as shown in Figure 2. Once the ferrite start temperature decreases, i.e. at the corresponding higher cooling rates, the diffusivity is lower, so is the diffusion rate of carbon. Therefore, more time is required to complete the austenite-to-ferrite transformation and the coexisting IP. Molybdenum is shown to have a more pronounced retardation of the ferritic transformation even at higher temperatures, where carbon diffusivity is high. This is due to the effect of Mo on lowering the activity of carbon and applying a stronger solute drag effect, also supported by other authors for vanadium-containing steels [26, 50]. Pearlite is formed for all compositions in applied cooling rates at about 12.00–0.75 Ks^{-1} for V25, 4.00–0.12 Ks^{-1} for V50, 1.63–0.10 Ks^{-1} for V50Mo, and 10.00–0.33 Ks^{-1} for V100, with an approximately constant fraction of only 1 to 3% (based on optical evaluation of the metallographic area fractions).

4.2 | Precipitation of Secondary Phases

Most of the precipitates shown in Figure 5 are needle shaped and aligned in parallel lines. This shape and morphology are typical of IP. Usually, IP is reported to be nanometer sized [31], but some studies [51–53] reported a coarsening during longer holding at higher temperatures [54]. Additionally, it has been confirmed by EDX analysis that some of those precipitates are V-rich for 100V and V- and Mo-rich in 50VMo [36]. Previous studies have shown that IPs can form in vanadium-containing steels during continuous cooling at cooling rate as low as $0.06\,Ks^{-1}$ [55]. Therefore, IP is plausible and they might have coarsened during the slow cooling. Interestingly, some grains do not have any precipitates, while other areas are densely covered. This behavior could be attributed to the different orientation relationship of different ferrite grains with respect to austenite [54]. It has been shown that the promotion of interphase VC precipitate nucleation occurs at non- KS α/γ interface rather than in K–S interface [56]. On the other hand, it could be attributed due to a distribution of very fine precipitates that are not possible to observe in SEM, because those precipitates have maintained their coherency even after slow cooling due to low misfit of VCs with ferrite [25]. In addition, accumulations of precipitates surrounded by depleted areas generally occur when the alloying elements are not homogeneously distributed at the time of precipitation, but clusters of alloying elements are present. This could be an additional indication that the chemical composition was not sufficiently homogenized during the austenitization of the dilatometer samples, being more pronounced at V50 and V100, as discussed previously.

The hardness of the investigated alloys is a combined function of the presence of hard phases, ferrite grain size, and microalloying strengthening in ferrite [57]. There is an evident decrease of hardness with decreasing of cooling rate for all analyzed compositions according to Figure 6. This can be explained by a shift in matrix microstructure from harder phases such as martensite and a mixture of WF and B to PF, accompanied by a general increase of grain size, as observed in LOM images and supported by other authors [55]. In martensite, for example, the hardness is mostly caused by the high dislocation density [58]. Similarly, WF and B inherit high dislocation densities, resulting in higher hardness than polygonal ferrite [59]. The hardness peak at medium cooling rates could be attributed to the ferrite grain refinement, pearlite formation, or VC precipitation. The obtained ferrite grain refinement with increased V and C contents for the same cooling rate can be explained by a more pronounced pinning effect by undissolved VC precipitates, as calculated previously by Thermo-Calc. However, no effect of the grain size on the hardness was observed. Therefore, the contribution of this effect could not totally be responsible for such hardness values, as supported by other authors [60]. The obtained amount of pearlite is around 1%–3%, which also cannot solely explain this considerable hardness increase. In fact, V having a higher affinity for C than Fe, promotes more readily VC than Fe_3C (cementite). Since there is a small fraction of pearlite, this indicates that the majority of C was taken to promote a vanadium IPs, during the austenite-to-ferrite transformation, rather than pearlite. This points out to a nearly suppressive effect of V on pearlite formation, which could have a further positive outcome in the resulting formability of the steel [52] and a high volume fraction of finely distributed interphase VC precipitates. Contrarily to random vanadium precipitates that show up within already formed ferrite, i.e., at temperatures lower than ferrite finish temperature, IPs occur during the transformation from austenite to ferrite at the migrating phase boundary [56, 61]. Therefore, the ferrite finish temperature corresponds to the temperature at which the IP formation is over [16]. As shown in Figure 7, the hardness peaks for all compositions are reached at the same ferrite finish temperature, around 650°C regardless of C and V contents. This evidence points to IP and its considerable impact on hardness of the steels, as already reported by other authors [62]. However, the HV peak is higher with increasing C and V concentrations, reaching, according to linear regression calculated by [63], 50, 590, and 850 MPa for V25, V50, and V100, respectively. This fact could be explained by a higher supersaturation with higher C and V contents, combined with an increased carbon activity in ferrite due to increasing amounts of carbon, leading to a higher driving force for precipitation [46]. Both effects lead to more refined and densely distributed VC precipitates with increase of both C and V, as supported by SEM and earlier work on EDX investigations [36].

Additionally, the hardness peak of V100 at fourth fastest cooling rate, composed by polygonal ferrite and pearlite, is higher than the fully martensitic state, which can only be achieved by intensive precipitation hardening. A particularly pronounced drop in hardness can be observed in V50, V50Mo, and V100 at cooling rates $< 300\,Ks^{-1}$, as the transition from purely martensitic microstructure to bainitic or ferritic microstructure takes place. The hardness of V100 is comparable to that of V50 at the fastest cooling rate. This is unexpected since higher C content of V100 should lead to a harder martensite due to a higher dislocation density caused by higher carbon content [56]. This could happen probably due to similar martensite fractions in alloys and due to a higher resulting ferrite fraction of V100 on account of more undissolved carbides after forging, as calculated by Thermo-Calc, leading to similar hardness. The addition of molybdenum leads to a shift of HV peak toward slower cooling rates, making it also broader. The peak height of the composition with Mo results in a reduction by ≈15HV relative to the Mo-free alloy, probably attributed to coarser and fewer precipitates present in SEM. This effect can be explained by the retardation of carbide formation caused by the presence of molybdenum, also reported in vanadium-containing steels [26, 58].

5 | Conclusions

The phase transformation behavior of high-purity V and V–Mo steels was investigated as the first step to design thermal treatments suitable for the formation of IPs of higher number density and narrow size distribution in a ferritic matrix, with the aim of producing high-performance microalloyed steels. The following conclusions can be drawn.

1. At faster cooling rates, Widmanstätten ferrite is formed dominantly, followed by an increase of the polygonal ferrite fraction with a decrease of cooling rate, until it fully replaces the Widmanstätten ferrite microstructure.
2. Increasing vanadium and carbon content promotes the formation of a fully polygonal ferrite microstructure at faster cooling rates and, for the same cooling rate, to a more refined ferrite grain size, due to a rise in VC dissolution temperature and the resulting stronger pinning effect of austenite grain boundaries by undissolved VC particles.

3. Molybdenum addition retards the kinetics of austenite-to-ferrite transformation and leads to a reduced hardening effect during continuous cooling, due to its solute drag effect.

4. The more significant hardening effect at a ferrite finish temperature of 650°C with rising carbon and vanadium contents, the nearly suppressive effect on pearlite formation and the in-row precipitates shown in SEM support the presence of a large volume fraction of vanadium IPs.

Author Contributions

Anastasiya Tselikova: writing – original draft (lead), writing – review & editing (lead). **Jannik Zuraszek:** investigation (lead), supervision (equal). **Ulrich Krupp:** project administration (equal), writing – review & editing (supporting). **Rolf Schmidt:** resources (lead), supervision (equal), writing – review & editing (supporting). **Hardy Mohrbacher:** validation (equal), writing – review & editing (supporting). **Alexander Gramlich:** conceptualization (equal), supervision (lead), writing – original draft (equal), writing – review & editing (equal).

Acknowledgments

The presented work is supported by *Vantage Alloys AG*, located in Switzerland.

Open Access funding enabled and organized by Projekt DEAL.

Funding

The authors have nothing to report.

Conflicts of Interest

The authors declare no conflicts of interest.

Data Availability Statement

The data that support the findings of this study are available from the corresponding author upon reasonable request.

References

1. M. Takahashi, O. Kawano, T. Hayashida, R. Okamoto, and H. Taniguchi, "High Strength Hot-rolled Steel Sheets for Automobiles," *Nippon Steel Technical Report* (2003), No. 88, 07, 2–7.

2. R. Landolfo, "Lightweight Steel Framed Systems in Seismic Areas: Current Achievements and Future Challenges," *Thin Wall Struct* 140 (2019): 114–131, https://doi.org/10.1016/j.tws.2019.03.039.

3. R. C. Guo, J. Zhou, and Y. Shi, "Application of the High Strength Steel in the Automobile," *Advanced Materials Research* 748 (2013): 227–230, https://doi.org/10.4028/www.scientific.net/amr.748.227.

4. S. S. Sohn, H. Song, J.-H. Kwak, and S. Lee, "Dramatic Improvement of Strain Hardening and Ductility to 95% in Highly-Deformable High-Strength Duplex Lightweight Steels," *Scientific Reports* 7 (2017): 1927, https://doi.org/10.1038/s41598-017-02183-4.

5. S.-H. Kim, H. Kim, and N. J. Kim, "Brittle Intermetallic Compound Makes Ultrastrong Low-Density Steel with Large Ductility," *Nature* 518 (2015): 77–79, https://doi.org/10.1038/nature14144.

6. S. Jiang, H. Wang, Y. Wu, et al., "Ultrastrong Steel via Minimal Lattice Misfit and High-Density Nanoprecipitation," *Nature* 544 (2017): 460–464, https://doi.org/10.1038/nature22032.

7. B. B. He, B. Hu, H. W. Yen, et al., "High Dislocation Density–induced Large Ductility in Deformed and Partitioned Steels," *Science* 357 (2017): 1029–1032, https://doi.org/10.1126/science.aan0177.

8. T.-C. Lin, C. Cao, M. Sokoluk, et al., "Aluminum with Dispersed Nanoparticles by Laser Additive Manufacturing," *Nature Communications* 10 (2019): 4124, https://doi.org/10.1038/s41467-019-12047-2.

9. A. Devaraj, V. V. Joshi, A. Srivastava, et al., "A Low-Cost Hierarchical Nanostructured Beta-Titanium Alloy with High Strength," *Nature Communications* 7 (2016): 11176, https://doi.org/10.1038/ncomms11176.

10. L.-Y. Chen, J.-Q. Xu, H. Choi, et al., "Processing and Properties of Magnesium Containing a Dense Uniform Dispersion of Nanoparticles," *Nature* 528 (2015): 539–543, https://doi.org/10.1038/nature16445.

11. S. Tang, T. Xin, W. Xu, et al., "Precipitation Strengthening in an Ultralight Magnesium Alloy," *Nature Communications* 10 (2019): 1003, https://doi.org/10.1038/s41467-019-08954-z.

12. S. Zheng, R. Rementeria, W. Kan, et al., "Nanoparticle Enabled High Performance High Modulus Steels," *Scripta Materialia* 201 (2021): 113954, https://doi.org/10.1016/j.scriptamat.2021.113954.

13. H. Springer, C. Baron, A. Szczepaniak, V. Uhlenwinkel, and D. Raabe, "Stiff, Light, Strong and Ductile: Nano-Structured High Modulus Steel," *Scientific Reports* 7 (2017): 2757, https://doi.org/10.1038/s41598-017-02861-3.

14. S. Münstermann, Y. Feng, and W. Bleck, "Influencing Parameters on Elastic Modulus of Steels," *Canadian Metallurgical Quarterly* 53 (2014): 264–273, https://doi.org/10.1179/1879139514Y.0000000127.

15. A. Antoni-Zdziobek, M. Gospodinova, F. Bonnet, and F. Hodaj, "Solidification Paths in the Iron-Rich Part of the Fe–Ti–B Ternary System," *Journal of Alloys and Compounds* 657 (2016): 302–312, https://doi.org/10.1016/j.jallcom.2015.10.104.

16. E. Pereloma, D. Cortie, N. Singh, G. Casillas, and F. Niessen, *Materials Research Letters* 8 (2020): 341–347, https://doi.org/10.1080/21663831.2020.1764121.

17. D. Raabe, B. Sun, A. Kwiatkowski Da Silva, et al., "Current Challenges and Opportunities in Microstructure-Related Properties of Advanced High-Strength Steels," *Metallurgical and Materials Transactions A* 51 (2020): 5517–5586, https://doi.org/10.1007/s11661-020-05947-2.

18. D. Raabe, C. C. Tasan, and E. A. Olivetti, "Strategies for Improving the Sustainability of Structural Metals," *Nature* 575 (2019): 64–74, https://doi.org/10.1038/s41586-019-1702-5.

19. J. Cong, J. Li, J. Fan, et al., "The Impact of Interphase Precipitation on the Mechanical Behavior of Fire-Resistant Steels at an Elevated Temperature," *Materials* 13 (2020): 4294, https://doi.org/10.3390/ma13194294.

20. Z. Xie, Z. Song, K. Chen, et al., "Study of Nanometer-Sized Precipitation and Properties of Fire Resistant Hot-Rolled Steel," *Metals* 9 (2019): 1230, https://doi.org/10.3390/met9111230.

21. Z. A. Guenechea and S. E. Offerman, *Critical Materials* (World Scientific, 2018), 5, 193–221, https://doi.org/10.1142/9789813271050_0010.

22. Z. Xiong, I. Timokhina, and E. Pereloma, "Clustering, Nano-Scale Precipitation and Strengthening of Steels," *Progress in Materials Science* 118 (2021): 100764, https://doi.org/10.1016/j.pmatsci.2020.100764.

23. C. Ioannidou, Z. Arechabaleta, A. Navarro-López, et al., "Interaction of Precipitation with Austenite-to-Ferrite Phase Transformation in Vanadium Micro-Alloyed Steels," *Acta Materialia* 181 (2019): 10–24, https://doi.org/10.1016/j.actamat.2019.09.046.

24. S. Ohkita and Y. Horii, "Recent Development in Controlling the Microstructure and Properties of Low Alloy Steel Weld Metals.," *ISIJ International* 35 (1995): 1170–1182, https://doi.org/10.2355/isijinternational.35.1170.

25. F. Azhari, A. Heidarpour, X.-L. Zhao, and C. R. Hutchinson, " Post-Fire Mechanical Response of Ultra-high Strength (Grade 1200) Steel Under High Temperatures: Linking Thermal Stability and Microstructure," *Thin Wall Struct* 119 (2017): 114–125, https://doi.org/10.1016/j.tws.2017.05.030.

26. P. Gong, X. G. Liu, A. Rijkenberg, and W. M. Rainforth, "The Effect of Molybdenum on Interphase Precipitation and Microstructures in Microalloyed Steels Containing Titanium and Vanadium," *Acta Materialia* 161 (2018): 374–387.

27. S. Lv, H.-H. Wu, K. Wang, et al., "The Austenite to Polygonal Ferrite Transformation in Low-Alloy Steel: Multi-Phase-Field Simulation," *Journal of Materials Research and Technology* 24 (2023): 9630–9643, https://doi.org/10.1016/j.jmrt.2023.05.192.

28. G. Krauss and S. W. Thompson, "Ferritic Microstructures in Continuously Cooled Low- and Ultralow-Carbon Steels.," *ISIJ International* 35 (1995): 937–945, https://doi.org/10.2355/isijinternational.35.937.

29. I. Schindler, J. NěmecP. Kawulok, et al., "The Combined Effect of Chemical Composition and Cooling Rate on Transformation Temperatures of Hypoeutectoid Steels," *Kovové materiály* 56, no. 03 (2018): 163–170, https://doi.org/10.4149/km_2018_3_163.

30. C. Ioannidou, A. Navarro-López, R. M. Dalgliesh, et al., "Phase-Transformation and Precipitation Kinetics in Vanadium Micro-Alloyed Steels by in-Situ, Simultaneous Neutron Diffraction and SANS," *Acta Materialia* 220 (2021): 117317, https://doi.org/10.1016/j.actamat.2021.117317.

31. N. Kamikawa, Y. Abe, G. Miyamoto, Y. Funakawa, and T. Furuhara, "Tensile Behavior of Ti,Mo-Added Low Carbon Steels with Interphase Precipitation," *ISIJ International* 54 (2014): 212–221, https://doi.org/10.2355/isijinternational.54.212.

32. Y.-J. Zhang, G. Miyamoto, K. Shinbo, and T. Furuhara, "Quantitative Measurements of Phase Equilibria at Migrating α/γ Interface and Dispersion of VC Interphase Precipitates: Evaluation of Driving Force for Interphase Precipitation," *Acta Materialia* 128 (2017): 166–175, https://doi.org/10.1016/j.actamat.2017.02.020.

33. Y. Zhang, G. Miyamoto, and T. Furuhara, "Enhanced Hardening by Multiple Microalloying in Low Carbon Ferritic Steels with Interphase Precipitation," *Scripta Materialia* 212 (2022): 114558, https://doi.org/10.2139/ssrn.3968007.

34. O. Arnold, J. C. Bilheux, J. M. Borreguero, et al., "Mantid—Data Analysis and Visualization Package for Neutron Scattering and μ SR Experiments," *Nuclear Instruments and Methods in Physics Research Section A* 764 (2014): 156–166, https://doi.org/10.1016/j.nima.2014.07.029.

35. M. Akhlaghi, T. Steiner, S. R. Meka, and E. J. Mittemeijer, "Misfit-Induced Changes of Lattice Parameters in Two-Phase Systems: Coherent/Incoherent Precipitates in a Matrix," *Journal of Applied Crystallography* 49 (2016): 69–77, https://doi.org/10.1107/S1600576715022608.

36. A. Tselikova, A. Gramlich, R. Schmidt, and U. Krupp, *Microalloying '25: International Symposium on Microalloying* (Association for Iron & Steel Technology, 2–5 June 2025). 152–160.

37. Y. Zheng, F. Wang, C. Li, Y. Li, J. Cheng, and R. Cao, "Effect of microstructure and precipitates on mechanical properties of Cr–Mo–V alloy steel with different austenitizing temperatures," *ISIJ International* 58 (2018): 1126–1135.

38. P. Petkov, *Austenite Decomposition of Low Carbon High Strength Steels During Continuous Cooling (T)*, (University of British Columbia, 2004), https://open.library.ubc.ca/collections/ubctheses/831/items/1.0078643.

39. E. A. Wilson, "The .GAMMA..RAR..ALPHA. Transformation in Low Carbon Irons.," *ISIJ International* 34 (1994): 615– 630, https://doi.org/10.2355/isijinternational.34.615.

40. W. Bleck, *Materials Science of Steel: Textbook for RWTH Aachen University Students*, 3rd reviseded. (IEHK, RWTH Aachen University, 2013)

41. R. L. Bodnar and S. S. Hansen, "Effects of Austenite Grain Size and Cooling Rate on Widmanstätten Ferrite Formation in Low-Alloy Steels," *Metallurgical and Materials Transactions A* 25 (1994): 665–675, https://doi.org/10.1007/BF02665443.

42. I. Loginova, J. Ågren, and G. Amberg, "On the Formation of Widmanstätten Ferrite in Binary Fe–C– Phase-Field Approach," *Acta Materialia* 52 (2004): 4055–4063, https://doi.org/10.1016/j.actamat.2004.05.033.

43. Y. Shao, C. Liu, Z. Yan, H. Li, and Y. Liu, "Formation Mechanism and Control Methods of Acicular Ferrite in HSLA Steels: A Review," *Journal of Materials Science & Technology* 34 (2018): 737–744, https://doi.org/10.1016/j.jmst.2017.11.020.

44. M. Umemoto, Z. Hai Guo, and I. Tamura, "Effect of Cooling Rate on Grain Size of Ferrite in a Carbon Steel," *Materials Science and Technology* 3 (1987): 249–255, https://doi.org/10.1179/mst.1987.3.4.249.

45. S. W. Thompson, D. J. Vin Col, and G. Krauss, "Continuous Cooling Transformations and Microstructures in a Low-Carbon, High-Strength Low-Alloy Plate Steel," *Metallurgical Transactions A* 21 (1990): 1493–1507, https://doi.org/10.1007/BF02672564.

46. S. Zajac, T. Siwecki, W. B. Hutchinson, and R. Lagneborg, "Strengthening Mechanisms in Vanadium Microalloyed Steels Intended for Long Products.," *ISIJ International* 38 (1998): 1130–1139, https://doi.org/10.2355/isijinternational.38.1130.

47. K.-S. Kim, L.-X. Du, and C.-R. Gao, "Influence of Vanadium Content on Bainitic Transformation of a Low-Carbon Boron Steel During Continuous Cooling," *Acta Metallurgica Sinica (English Letters)* 28 (2015): 692–698, https://doi.org/10.1007/s40195-015-0249-1.

48. F. Ishikawa, T. Takahashi, and T. Ochi, "Intragranular Ferrite Nucleation in Medium-Carbon Vanadium Steels," *Metallurgical and Materials Transactions A* 25 (1994): 929–936, https://doi.org/10.1007/BF02652268.

49. G. Miyamoto, R. Hori, B. Poorganji, and T. Furuhara, "Interphase Precipitation of VC and Resultant Hardening in V-Added Medium Carbon Steels," *ISIJ International* 51 (2011): 1733–1739, https://doi.org/10.2355/isijinternational.51.1733.

50. P. Uranga, C.-J. Shang, T. Senuma, J.-R. Yang, A.-M. Guo, and H. Mohrbacher, "Molybdenum Alloying in High-performance Flat-rolled Steel Grades," *Advances in Manufacturing* 8 (2020): 15–34.

51. M. Nöhrer, S. Zamberger, S. Primig, and H. Leitner, "Atom Probe Study of Vanadium Interphase Precipitates and Randomly Distributed Vanadium Precipitates in Ferrite," *Micron* 54-55 (2013): 57–64, https://doi.org/10.1016/j.micron.2013.08.008.

52. Y. Q. Wang, S. J. Clark, V. Janik, et al., "Investigating Nano-Precipitation in a V-Containing HSLA Steel Using Small Angle Neutron Scattering," *Acta Materialia* 145 (2018): 84–96, https://doi.org/10.1016/j.actamat.2017.11.032.

53. Y.-J. Zhang, G. Miyamoto, K. Shinbo, and T. Furuhara, "Effects of α/γ Orientation Relationship on VC Interphase Precipitation in Low-Carbon Steels," *Scripta Materialia* 69 (2013): 17–20, https://doi.org/10.1016/j.scriptamat.2013.03.020.

54. A. Karmakar, P. Sahu, S. Neogy, et al., "Effect of Cooling Rate and Chemical Composition on Microstructure and Properties of Naturally Cooled Vanadium-Microalloyed Steels," *Metallurgical and Materials Transactions A* 48 (2017): 1581–1595, https://doi.org/10.1007/s11661-017-3964-6.

55. M. M. A. Bepari, "Structure of Continuously Cooled Low-Carbon Vanadium Steels," *Metallurgical Transactions A* 21 (1990): 2839–2855, https://doi.org/10.1007/BF02647205.

56. S. Morito, J. Nishikawa, and T. Maki, "Dislocation Density Within Lath Martensite in Fe-C and Fe-Ni Alloys," *ISIJ International* 43 (2003): 1475– 1477, https://doi.org/10.2355/isijinternational.43.1475.

57. A. Bhattacharya, K. Ankit, and B. Nestler, "Phase-Field Simulations of Curvature-Induced Cascading of Widmanstätten-Ferrite Plates," *Acta Materialia* 123 (2017): 317–328, https://doi.org/10.1016/j.actamat.2016.10.035.

58. A. Gramlich, A. Middleton, R. Schmidt, and U. Krupp, "On the Influence of Vanadium on Air-Hardening Medium Manganese Steels for Sustainable Forging Products," *Steel Research International* 92 (2021): 2000592, https://doi.org/10.1002/srin.202000592.

59. A. Barbacki and R. W. K. Honeycombe, "Transitions in Carbide Morphology in Molybdenum and Vanadium Steels," *Metallography* 9 (1976): 277–291, https://doi.org/10.1016/0026-0800(76)90054-9.

60. N. K. Balliger and R. W. K. Honeycombe, "The Effect of Nitrogen on Precipitation and Transformation Kinetics in Vanadium Steels," *Metallurgical Transactions A* 11 (1980): 421–429, https://doi.org/10.1007/BF02654566.

61. T. N. Baker, "Microalloyed Steels," *Ironmaking & Steelmaking* 43 (2016): 264–307, https://doi.org/10.1179/1743281215Y.0000000063.

62. Y.-J. Zhang, G. Miyamoto, K. Shinbo, et al., "Effects of Transformation Temperature on VC Interphase Precipitation and Resultant Hardness in Low-Carbon Steels," *Acta Materialia* 84 (2015): 375–384, https://doi.org/10.1016/j.actamat.2014.10.049.

63. E. Pavlina and C. Van Tyne, "Correlation of Yield Strength and Tensile Strength with Hardness for Steels" *Journal of Materials Engineering and Performance* 17 (2008): 888–893, https://doi.org/10.1007/s11665-008-9225-5.

Appendix

TABLE A1 | Applied cooling rates and $t_{8/5}$ for steel V25.

Sample number	$_{8/5}t$ -time, s	Cooling rate, K/s
1	1	300.00
2	2.78	107.90
3	5.64	53.20
4	12.38	24.20
5	25	12.00
6	50	6.00
7	100	3.00
8	200	1.50
9	400	0.75
10	800	0.38
11	1600	0.19
12	3200	0.09
13	6400	0.05

TABLE A2 | Applied cooling rates and $t_{8/5}$ for steel V50.

Sample number	$_{8/5}t$ -time, s	Cooling rate, K/s
1	1.05	285.71
2	2.67	112.36
3	5.43	55.25
4	9.48	31.65
5	19	15.79
6	38	7.89
7	76	3.95
8	152	1.97
9	304	0.99
10	608	0.49
11	1216	0.25
12	2432	0.12
13	4864	0.06
14	9728	0.03

TABLE A3 | Applied cooling rates and $t_{8/5}$ for steel V50Mo.

Sample number	$_{8/5}t$ -time, s	Cooling rate, K/s
1	0.97	309.28
2	2.73	109.89
3	5.05	59.41
4	11.24	26.69
5	23	13.04
6	46	6.52
7	92	3.26
8	184	1.63
9	368	0.82
10	736	0.41
11	1472	0.20
12	2944	0.10
13	5888	0.05
14	11 776	0.03

TABLE A4 | Applied cooling rates and $t_{8/5}$ for steel V100.

Sample number	$_{8/5}t$ -time, s	Cooling rate, K/s
1	0.99	303.03
2	1.97	152.28
3	4.29	69.93
4	13.16	22.80
5	28	10.71
6	56	5.36
7	112	2.68
8	224	1.34
9	448	0.67
10	896	0.33
11	1792	0.17
12	3584	0.08
13	7168	0.04